




 Cite this: *Phys. Chem. Chem. Phys.*,  
2023, 25, 30237

# High-field and fast-spinning $^1\text{H}$ MAS NMR spectroscopy for the characterization of two-dimensional covalent organic frameworks†

 Nikolaj Lopatik,<sup>a</sup> Ankita De,<sup>b</sup> Silvia Paasch,<sup>a</sup> Andreas Schneemann <sup>b</sup> and Eike Brunner <sup>\*a</sup>

Two-dimensional (2D) materials, like 2D covalent organic frameworks (COFs), have been attracting increasing research interest. They are usually obtained as polycrystalline powders. Solid-state NMR spectroscopy is capable of delivering structural information about such materials. Previous studies have applied, for example,  $^{13}\text{C}$  cross-polarization magic angle spinning (CP MAS) NMR experiments to characterize 2D COFs. Herein, we demonstrate the usefulness of high-field and fast-spinning  $^1\text{H}$  MAS NMR spectroscopy to resolve and quantify the signals of different  $^1\text{H}$  species within 2D COFs, including the edge sites and/or defects. Moreover,  $^1\text{H}$ – $^{13}\text{C}$  heteronuclear correlation (HETCOR) spectroscopy has also been applied and can provide improved resolution to obtain further information about stacking effects as well as edge sites/defects.

 Received 28th August 2023,  
Accepted 16th October 2023

DOI: 10.1039/d3cp04144a

rsc.li/pccp

## 1. Introduction

The synthesis of graphene<sup>1</sup> and its chemical modifications, such as graphene oxide,<sup>2,3</sup> has paved the way towards various new two-dimensional materials (2DMs).<sup>4–21</sup> Meanwhile, 2D materials/layered materials, like boron nitride,<sup>4</sup> silicene,<sup>5</sup> germanene,<sup>6</sup> stanene,<sup>7</sup> and phosphorene,<sup>8</sup> have been synthesized. Two-dimensional versions of metal-carbides and nitrides, the so-called MXenes,<sup>9–11</sup> have proven to be useful materials in the field of energy storage and conversion. Likewise, 2D materials constructed from molecular building blocks, such as metal–organic frameworks (MOFenes)<sup>12</sup> and covalent organic frameworks (COFs), are finding increasing research interest,<sup>13–21</sup> with potential applications in ion storage, separation technology, and energy conversion. Layered COF syntheses usually provide polycrystalline powders that suffer from low crystallinity.<sup>22</sup> This makes the detailed structural description of their short-range order challenging and requires often a reliance on computation.<sup>21</sup> The delamination of these layered materials further decreases the applicability of X-ray diffraction-based techniques for structure determination.

Parallel to these synthesis efforts, solid-state NMR spectroscopy<sup>23</sup> is increasingly used to investigate COFs/2D COFs and other 2D materials<sup>3,11,24–33</sup> in order to mitigate the inherent shortcomings of other commonly used characterization techniques. Although techniques like NEXAFS (near-edge X-ray absorption fine structure) in principle also allow the determination of the closer environment of atoms, they fail for example for hydrogen or other light elements with a low number of electrons. Solid-state NMR spectroscopy relies on the detection of nuclear spins, like  $^1\text{H}$ ,  $^{13}\text{C}$ , or others acting as local probes. The short-range interactions of these spins, like the shielding (chemical shift) caused by electrons in the neighborhood of the considered nuclei, the magnetic dipole–dipole interaction with neighboring nuclear spins, and others are then exploited to obtain structural information. Furthermore, the application of solid-state NMR spectroscopy does not necessarily require crystalline samples and is thus very helpful to study COFs, including 2D COFs.  $^{11}\text{B}$  magic angle spinning (MAS) NMR spectroscopy was used to prove the formation of boron-containing heterocycles in COF-1 (boroxine) and COF-5 (boronate ester) by the line-shape analysis of the second-order quadrupole broadened  $^{11}\text{B}$  signals.<sup>24</sup>  $^{13}\text{C}$  MAS NMR spectroscopy – usually combined with  $^1\text{H}$ – $^{13}\text{C}$  cross-polarization (CP) – is meanwhile a standard characterization technique for graphene oxide and its functionalized variants,<sup>3,25–27</sup> as well as for COFs.<sup>28–32</sup> It allows, for example, monitoring imine bond formation and imine protonation during COF syntheses by  $^{13}\text{C}$  chemical shift analysis.<sup>28,29</sup> Recently,  $^{13}\text{C}$  CP MAS NMR spectroscopy

<sup>a</sup> Chair of Bioanalytical Chemistry, Faculty of Chemistry and Food Chemistry, TU Dresden, 01062 Dresden, Germany. E-mail: eike.brunner@tu-dresden.de

<sup>b</sup> Chair of Inorganic Chemistry I, Faculty of Chemistry and Food Chemistry, TU Dresden, 01062 Dresden, Germany

† Electronic supplementary information (ESI) available. See DOI: <https://doi.org/10.1039/d3cp04144a>

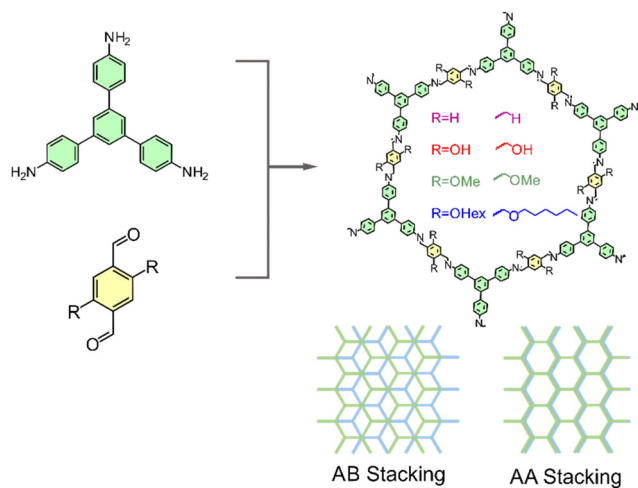


Fig. 1 Structure of the monomers TAB and TA-R used for the synthesis (left); structure of the obtained 2D COFs (top right); and proposed layer stacking modes (bottom, right).

was used to derive information about the layer stacking in 2D COFs.<sup>32</sup>

The present contribution shows that  $^1\text{H}$  MAS NMR spectroscopy at high magnetic fields and sample spinning rates is another useful technique for the structure determination of 2D COFs. It allows signal resolution and the quantification of different  $^1\text{H}$  species in intact samples, which in previous studies was only possible by decomposition of the COFs.<sup>34</sup> Additionally, it has also been demonstrated that  $^{13}\text{C}$  CP MAS NMR experiments do not necessarily require high fields and sample spinning rates. Furthermore,  $^1\text{H}$ - $^{13}\text{C}$  HETCOR can help elucidate the proximities between carbons and protons as well as stacking effects. As a model system, we chose four structurally related 2D layered COF materials, namely **TAB-TA**, **TAB-TA-OH**, **TAB-TA-OMe**, and **TAB-TA-OHex** (cf. Fig. 1).

Here, materials were synthesized by the condensation reaction of the tritopic amine functionalized linker TAB (TAB = 1,3,5-tris(4-aminophenyl)benzene) and the ditopic aldehydes TA-H (terephthalic aldehyde), TA-OH (2,5-dihydroxyterephthalic aldehyde), TA-OMe (2,5-dimethoxyterephthalic aldehyde), and TA-OHex (2,5-dihexoxyterephthalic aldehyde).<sup>14</sup> These isostructural compounds with different substitution patterns on the aldehyde linker were speculated to have different interlayer interactions. From an energetic viewpoint, the interlayer van der Waals interactions, especially the balance between the London dispersion interactions among nonpolar groups and the Coulomb forces caused by polar connector groups interaction, determine the stacking patterns in 2D COFs.<sup>16</sup>

## 2. Experimental

### Materials synthesis

1,3,5-Tris(4-aminophenyl)benzene was synthesized according to a previously reported procedure.<sup>35</sup> Terephthalaldehyde (>98%) and 2,5-dimethoxyterephthalaldehyde (>97%) were

obtained from Sigma Aldrich. Other reagents and solvents were obtained from commercial sources and used as received.

### Linker synthesis

$^1\text{H}$  NMR data of all the used linkers are provided in the ESI,<sup>†</sup> see Fig. S1–S4.

### Synthesis of 2,5-dihydroxyterephthalaldehyde

2,5-Dimethoxyterephthalaldehyde (190 mg, 1.00 mmol) was dissolved in 16 mL anhydrous dichloromethane (DCM). The reaction mixture was then cooled down to 0 °C.  $\text{BBr}_3$  solution (0.6 mL) diluted with 4 mL anhydrous DCM was added dropwise to the reaction mixture under inert conditions. Thereafter, the reaction mixture was stirred continuously for 12 h at room temperature. The reaction mixture was subsequently subjected to vacuum to remove the volatiles. The solid residue was then quenched by the addition of 20 mL of a mixture of  $\text{H}_2\text{O}/\text{MeOH}$  (4:1). The product was then extracted with ethyl acetate (200 mL), washed with brine, and dried over  $\text{MgSO}_4$ . The organic layer was then filtered and evaporated and afterwards dried *in vacuo* and recrystallized from ethyl acetate. The product was then separated and washed with DCM and heptane and dried under vacuum, yielding the compound as a yellow powder.<sup>36</sup> Yield: 120 mg (0.72 mmol, 73%);  $^1\text{H}$  NMR: (DMSO- $d_6$ , 300 MHz):  $\delta$  = 10.39 (s, 2 H; -CHO), 10.36 (s, 2 H; -OH), 7.23 (s, 2 H; ArH).

### Synthesis of 2,5-dihexoxyterephthalaldehyde

To a solution of 0.166 g (0.99 mmol, 1 eq.) of 2,5-dihydroxyterephthalaldehyde in 5 mL DMF, 0.415 g of  $\text{K}_2\text{CO}_3$  (3.00 mmol) and 0.495 g (3.00 mmol, 3 eq.) of 1-bromohexane were added and stirred at 90 °C overnight. After cooling to room temperature, the mixture was poured into 100 mL water and extracted with ethylacetate. The organic phase was dried over  $\text{MgSO}_4$  and the solvent was evaporated in vacuum. A brown oily liquid was obtained, which was purified *via* column chromatography using 4:1 hexane:ethylacetate to give a yellow powder. Yield: 220 mg (0.66 mmol, 65.8%).  $^1\text{H}$  NMR (300 MHz, DMSO- $d_6$ ):  $\delta$  = 10.40 (s, 1H), 7.41 (s, 1H), 4.13 (s, 2H), 1.76 (s, 2H), 1.38 (d,  $J$  = 37.6 Hz, 6H), 0.87 (s, 3H).

### COF synthesis

A solvothermal synthetic approach was used for this Schiff base condensation reaction between 1,3,5-tris(4-aminophenyl)benzene (0.095 mmol) as the tritopic linker and terephthalaldehyde (TA) or 2,5 substituted terephthalaldehyde (TA-OH, TA-OMe, or TA-OHex) (0.143 mmol) as the ditopic linkers.<sup>15</sup> The linkers were dispersed in a mixture of 1,4-dioxane:mesitylene (4:1, 1 mL), and acetic acid (6 M (aq.), 0.2 mL) within a borosilicate ampoule. The ampoule was flash-frozen in a liquid nitrogen bath three times while applying a vacuum in order to degas the solvent, and it was then flame-sealed. It was then sonicated for homogenous mixing of all the components and then kept at 120 °C for 3 days in an isothermal oven. After cooling to room temperature, the ampoule was opened and the formed solid was filtered off and then transferred into a

thimble for Soxhlet extraction. The material was Soxhlet extracted with THF and subsequently with ethanol, and afterwards supercritically dried to remove ethanol (see below for details). After activation, the samples were transferred into an argon-filled glovebox and stored there for further measurements.

The supercritical drying procedure was performed in a Jumbo Critical Point Dryer 13200JAB (SPI Supplies). Prior to the supercritical drying process, all the samples were solvent exchanged to ethanol and placed in filter crucibles. The filter crucibles containing the samples were placed in a cooled autoclave (17 °C). The chamber was filled with liquid CO<sub>2</sub> and purged for 4 days. The temperature was then raised to 37 °C, resulting in a chamber pressure of around 90 bar. The pressure was released to transfer the samples into the glovebox and were then further handled under an inert gas atmosphere.

### Characterization

The quality and purity of the synthesized COF samples were evaluated using standard characterization methods as described below prior to the analysis by solid-state NMR spectroscopy. Powder X-ray diffraction (PXRD) measurements verified the crystallinity and exhibited reflections matching the simulated patterns (Fig. S5, ESI†). FTIR measurements revealed the disappearance of the N–H stretching at 3430 cm<sup>-1</sup> and the carbonyl band at 1680 cm<sup>-1</sup> for the linkers accompanied by the appearance of imine bond vibrations at 1610 cm<sup>-1</sup> (Fig. S6, ESI†), indicating the successful synthesis. C–H stretching bands also appeared at approximately 3000 cm<sup>-1</sup> for the **TAB-TA-OHex** COF and the corresponding linker, suggesting that the included side groups were intact. The conducted nitrogen physisorption experiments verified the porous nature of the compounds (Fig. S7, ESI†) having surface areas ( $S_{\text{BET}}$ ) of 498.5 m<sup>2</sup> g<sup>-1</sup> for **TAB-TA-OHex**,<sup>37</sup> 1773.1 m<sup>2</sup> g<sup>-1</sup> for **TAB-TA-OMe**,<sup>38</sup> 1840.4 m<sup>2</sup> g<sup>-1</sup> for **TAB-TA-OH**,<sup>39</sup> and 1184.7 m<sup>2</sup> g<sup>-1</sup> for **TAB-TA**.<sup>38</sup> The SEM images revealed the morphology as spherical crystalline aggregates (Fig. S8, ESI†).

### Powder X-ray diffraction

Powder X-ray diffraction (PXRD) patterns were recorded on a STOE StadiP in 2 $\theta$  Bragg–Brentano geometry using Cu K $\alpha$ 1 ( $\lambda$  = 1.5405 Å) radiation and a 2D detector (Mythen, Dectris) in the transmission mode. The patterns were collected in the 2 $\theta$  range of 2°–50° with a scan speed of 150 s per step. For the measurements, the samples were put into a custom-built stainless-steel sample holder, which consisted of a stainless-steel plate with *ca.* 1 mm aperture. The COF powders were pressed into the aperture. This setup allowed us to minimize the background noise within the recorded powder XRD patterns.

### Physisorption experiments

Nitrogen physisorption experiments were carried out using a Quadrasorb SI instrument. The materials were previously activated using supercritical CO<sub>2</sub> and the sample cell was filled inside an argon glovebox with 20–40 mg of material. Brunauer–Emmett–Teller (BET) surface areas were calculated from the

linear region of the N<sub>2</sub> isotherm at 77 K using AsiQwin software within the pressure range  $p/p_0$  of 0.04–0.12.

### Scanning electron microscopy (SEM)

SEM images were taken with secondary electrons in a HITACHI SU8020 microscope using a 2.0 kV acceleration voltage and 8 mm working distance. The sample was dispersed in ethanol by thorough sonication and dropcast on a silicon wafer. It was then fixed to the sample holder by a carbon pad. Thereafter, the samples were sputtered with gold to increase the conductivity.

### Fourier-transform infrared spectroscopy

The FT-IR spectra were measured on a Bruker VERTEX 70 in the range of 4000–600 cm<sup>-1</sup> in the ATR mode. All the measured spectra were background corrected.

### Solid-state NMR experiments

Solid-state NMR experiments were carried out using 300 MHz and 800 MHz Bruker Avance spectrometers. Measurements on the 300 MHz spectrometer were performed using a commercial 2.5 mm double-resonance magic angle spinning (MAS) probe at a 15 kHz sample spinning rate. Measurements on the 800 MHz spectrometer were recorded using a 1.3 mm double-resonance magic angle spinning (MAS) probe at different sample spinning rates up to 60 kHz. The <sup>1</sup>H MAS NMR spectra were recorded by direct excitation with a delay of 3 s between subsequent scans. The background signal of the probe was subtracted as demonstrated in the ESI† (*cf.* Fig. S9). The <sup>13</sup>C CP MAS NMR spectra were recorded by ramped CP with <sup>1</sup>H decoupling (SPINAL-64) and a 3 s delay between subsequent scans. Spectra were referenced relative to TMS using adamantane as the secondary reference.

Chemical shift predictions were obtained by the software ACD Labs.<sup>40</sup> This software uses two algorithms: a hierarchically ordered spherical environment (HOSE) and neural network. The HOSE code is a well-known method for representing the chemical surroundings of a specific atom up to a predetermined number of bonds. Shifts for structures that are not represented in the database are predicted better by neural network algorithms.

<sup>1</sup>H–<sup>13</sup>C HETCOR spectra were acquired at 800 MHz <sup>1</sup>H resonance frequency and a 50 kHz sample spinning rate using <sup>13</sup>C detection, *i.e.*, the well-resolved <sup>13</sup>C dimension was directly detected. The <sup>1</sup>H dimension with its intrinsically lower resolution was chosen as the indirect dimension. Heteronuclear polarization transfer was achieved by ramped cross-polarization at a 4 ms CP contact time. Overall, 80–180 scans were added with a recycle delay time of 3 s.

## 3. Results and discussion

### Optimization of the <sup>1</sup>H MAS NMR measurements

Fig. 2 displays the <sup>1</sup>H MAS NMR spectra of **TAB-TA-OH** measured at two different magnetic fields with flux densities of

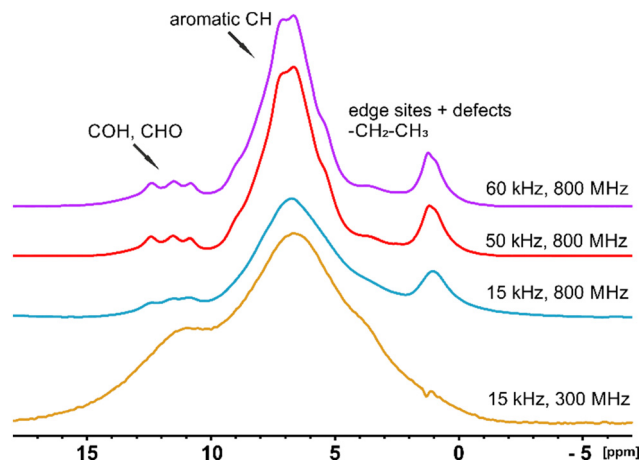


Fig. 2  $^1\text{H}$  MAS NMR spectra of **TAB-TA-OH** measured at variable sample spinning rates and two different magnetic fields with flux densities of 7.04 T and 18.79 T.

7.04 T and 18.79 T corresponding to 300 and 800 MHz  $^1\text{H}$  resonance frequency, respectively.

The spectra recorded at 800 MHz resonance frequency were, furthermore, acquired under variation of the sample spinning rate from 15 kHz to 60 kHz. Notably, the spectral resolution was considerably improved by both, the higher magnetic field strength and the increasing sample spinning rate  $\nu_r$  up to 60 kHz, allowing resolution of various signals as assigned in the figure. The reason for this behavior is the dominating influence of homonuclear  $^1\text{H}$ - $^1\text{H}$  dipole-dipole coupling in the proton-rich 2D COF materials at lower sample spinning rates. This homogeneous line broadening mechanism causes a spinning-rate-dependent residual linewidth of MAS NMR signals,  $\Delta\nu_{1/2}^{\text{MAS}}$ , described by eqn (1) below.<sup>41,42</sup>

$$\Delta\nu_{1/2}^{\text{MAS}} = \frac{1}{A} \frac{(\Delta\nu_{\parallel})^2}{\nu_r} \quad (1)$$

Here,  $\Delta\nu_{\parallel}$  denotes the homonuclear contribution to the static linewidth (*i.e.*, without MAS), which can be determined from the second moment contribution due to homonuclear  $^1\text{H}$ - $^1\text{H}$  dipole-dipole coupling. The parameter  $A$  depends on the spin system geometry.<sup>41,42</sup> The residual linewidth  $\Delta\nu_{1/2}^{\text{MAS}}$  measured in frequency units is independent of the external magnetic field. Hence, the spectral resolution increases at the ppm scale with increasing the external field strength. Furthermore, an increasing sample spinning rate is accompanied by a decreasing residual linewidth, *i.e.*, further increasing the resolution as long as the homonuclear contribution described by eqn (1) is not sufficiently averaged out. These effects are demonstrated in Fig. 2. At sufficiently high sample spinning rates; however, other line broadening effects dominate. For highly anisotropic materials like 2D COFs, we anticipated significant magnetic susceptibility anisotropies and that the MAS NMR signals of such samples would exhibit a residual line broadening even at very high sample spinning rates.<sup>43,44</sup> Note that the commonly measured  $^{13}\text{C}$  CP MAS NMR spectra behave differently because the homonuclear  $^{13}\text{C}$ - $^{13}\text{C}$  dipole-dipole interaction is rather

weak due to the low gyromagnetic ratio of  $^{13}\text{C}$  and its low natural abundance of only 1.1%. The resulting very weak homogeneous  $^{13}\text{C}$ - $^{13}\text{C}$  dipole-dipole interaction is averaged out even at relatively low sample spinning rates provided that the routinely used  $^1\text{H}$  decoupling is applied during signal acquisition to decouple the carbon spins from the strongly coupling proton spin bath. The residual linewidth is then also independent from  $B_0$  at the ppm scale (Fig. S10, ESI $^\dagger$ ). That means, the detection of the optimum resolved  $^{13}\text{C}$  CP MAS NMR spectra is already possible at relatively low field strengths and sample spinning rates.<sup>45</sup>

Based on chemical shift prediction using the software ACD Labs,<sup>40</sup> an assignment of the signals resolved at 800 MHz and sample spinning rates of 50 kHz or beyond could be suggested, as indicated in Fig. 2 and as described in full detail in the ESI $^\dagger$  (Fig. S12 and Table S2). The relatively broad and asymmetric main signal centered at around *ca.* 6.6 ppm represented aromatic CH groups and resulted from the various aromatic protons found in the structure. This could be decomposed into at least five lines, as shown in Fig. S12 (ESI $^\dagger$ ). The additional signals at low chemical shifts, *i.e.*, at *ca.* 3.4, 2.3, and 1.0 ppm, could be explained by  $\text{CH}_2$  and  $\text{CH}_3$  groups. Adsorbed solvent molecules were efficiently removed after the synthesis procedure as described in the Experimental section by solvent exchange with ethanol and subsequent critical point drying. This means, the latter signals were indicative of edge sites and/or defects that may have been formed during the synthesis procedure, *e.g.*, by side-reactions with solvent molecules. Furthermore, three relatively weak signals at 10.8, 11.5, and 12.4 ppm were resolved at high sample spinning rates and a fourth signal occurred as a weak shoulder at an even higher chemical shift (*cf.* the signal decomposition shown in ESI $^\dagger$  Fig. S12). The origin of these signals will be discussed in detail below. In conclusion,  $^1\text{H}$  MAS NMR experiments on 2D COFs, like the samples studied here, should be performed at high magnetic fields and sample spinning rates of at least 50 kHz or beyond.

### Comparison of the four different 2D COFs

Fig. 3 displays the  $^1\text{H}$  MAS NMR spectra of **TAB-TA**, **TAB-TA-OH**, **TAB-TA-OMe**, and **TAB-TA-OHex** measured at 800 MHz resonance frequency and a 50 kHz sample spinning rate. The signal of the aromatic  $^1\text{H}$  occurred as broad and poorly resolved line centered at 6.4–7.1 ppm for all the samples. In most cases, this line was not symmetric and/or exhibited shoulders indicating the presence of different aromatic sites that were, however, not fully resolved. This signal (denoted as line 1 in the following) was thus decomposed into different lines for the quantitative evaluation of the spectra (*cf.* ESI $^\dagger$  Fig. S11–S14). Comparison of the  $^1\text{H}$  MAS NMR spectra also revealed characteristic differences due to the different side groups R (*cf.* Fig. 1) as well as edge sites/defects.

**TAB-TA.** For the perfect and infinitely large 2D layers of **TAB-TA**, only aromatic  $^1\text{H}$  sites (signal 1) were expected. The corresponding broad and intense signal (line 1) was found at 7.1 ppm. In addition, the spectrum clearly revealed signals at

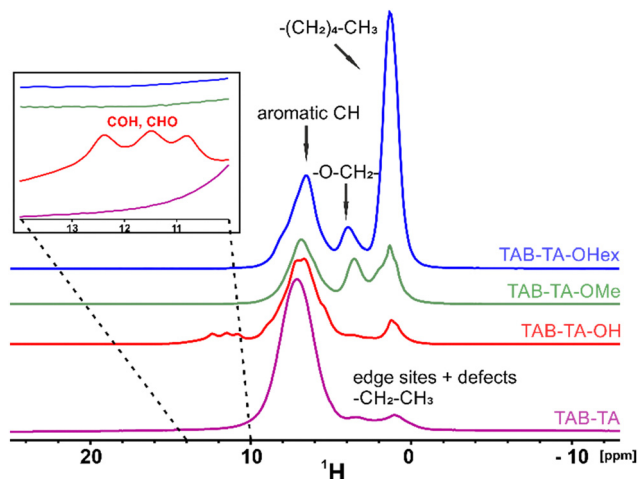


Fig. 3  $^1\text{H}$  MAS NMR spectra of **TAB-TA**, **TAB-TA-OH**, **TAB-TA-OMe**, and **TAB-TA-OHex** measured at 800 MHz resonance frequency and a 50 kHz sample spinning rate.

3.4 ppm (line 2), 2.4 ppm (line 3), and 1.0 ppm (line 4, Fig. S11, ESI<sup>†</sup>), which together represented *ca.* 9% of the total  $^1\text{H}$  intensity (Table S1, ESI<sup>†</sup>). These observations pose the question about which edge sites and/or defects would be possible for real 2D COFs of limited size. Incompletely cross-linked TAB molecules at the edges of the 2D layers would exhibit non-bonded  $\text{NH}_2$  groups possibly overlapping with the broad and intense signal at *ca.* 7 ppm due to the aromatic  $^1\text{H}$ . However,  $\text{NH}_2$  groups are rather reactive, and thus it was likely that  $\text{NH}_2$  reacted either with TA or with acetic acid, which was the catalyst for the imine bond formation and was present in excess within the synthesis mixture. The latter would result in covalently bound  $\text{N-CO-CH}_3$  moieties as edge sites. The chemical shift of this  $\text{CH}_3$  group would be expected around *ca.* 2 ppm. If TA molecules were not completely interconnected with TAB, they could exhibit unreacted CHO groups. Their  $^1\text{H}$  chemical shift would be expected around 10 ppm. If their number was relatively low, the corresponding signal may well be covered by the broad main signal due to the aromatic  $^1\text{H}$  sites. In this scenario,  $^{13}\text{C}$  CP MAS NMR spectroscopy was used (Fig. 4) in order to obtain further information about the possible edge/defect sites. Unreacted CHO moieties should give rise to a characteristic signal at *ca.* 192 ppm, which would be well separated from the dominating aromatic  $^{13}\text{C}$  signals. However, the spectrum of **TAB-TA** did not reveal a corresponding signal at this chemical shift. Together with the observations made by  $^1\text{H}$  MAS NMR spectroscopy, it could be concluded that the number of unreacted CHO moieties was low in **TAB-TA**. However, the observed signals at 3.4 and 1.0 ppm in **TAB-TA** were indicative of  $\text{O-CH}_2$  and  $\text{C-CH}_3$  groups. Such edge sites may form from initially unreacted CHO groups of TA molecules by a subsequent reaction with ethanol during solvent exchange (hemiacetal/acetal formation). In any case, it was concluded that the edge sites and/or other defects in **TAB-TA** were mainly aliphatic  $\text{CH}_2$  and  $\text{CH}_3$  groups.

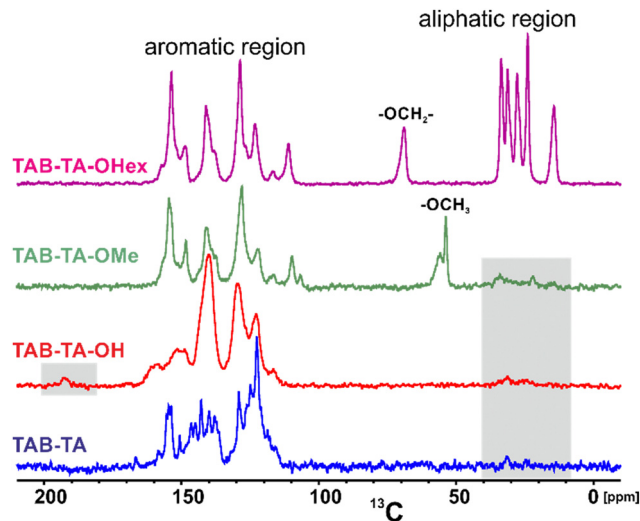


Fig. 4  $^{13}\text{C}$  CP MAS NMR spectra of **TAB-TA**, **TAB-TA-OH**, **TAB-TA-OMe**, and **TAB-TA-OHex** measured at 800 MHz resonance frequency and a 50 kHz sample spinning rate. (The signals that were not expected for a perfect and infinitely large 2D structure are highlighted in grey.)

This conclusion was supported by the presence of weak but detectable  $^{13}\text{C}$  signals in the aliphatic region for **TAB-TA** (*cf.* Fig. 4).

Note that the  $^{13}\text{C}$  CP MAS NMR spectrum of **TAB-TA** had a higher resolution than the other samples. Given the fact that all the samples exhibited high crystallinity (*cf.* ESI<sup>†</sup>, Fig. S5), the larger linewidth observed for the other samples could be explained by a lower degree of static and/or dynamic disorder in **TAB-TA**. Indeed, the number of defect and edge site protons observed for **TAB-TA** was relatively low compared to the other samples (*cf.* Table 1).

**TAB-TA-OH.** The center of gravity of the broad signal of the aromatic  $^1\text{H}$  sites (line 1) in **TAB-TA-OH** occurred at 6.8 ppm. In addition to this signal, lines at 10.8, 11.5, and 12.4 ppm were

Table 1 Quantitative evaluation of the  $^1\text{H}$  MAS NMR spectra of the different samples based on the signal decomposition shown in the ESI (Fig. S11–S14)

Compound	Line 1 <sup>a</sup>	Line 2 <sup>a</sup>	Line 3 <sup>a</sup>	Line 4 <sup>a</sup>
	$^1\text{H}^{\text{ar}}/\text{TAB}^{\text{b}}$	$^1\text{H}/\text{TAB}^{\text{b}}$	$^1\text{H}/\text{TAB}^{\text{b}}$	$^1\text{H}/\text{TAB}^{\text{b}}$
<b>TAB-TA</b>	24	0.5/—	0.5	1.8/—
<b>TAB-TA-OH</b>	21	1.9/—	—	4.0/—
<b>TAB-TA-OMe</b>	21	10.7/9	3.1	9.8/—
<b>TAB-TA-OHex</b>	21	6.5/6	—	34.3/33

<sup>a</sup> Signal assignment: line 1: aromatic  $^1\text{H}$  at 6.4–7.1 ppm. Note that the signal intensity of line 1 was set to the number of aromatic protons expected for the perfect structure; line 2:  $\text{O-CH}_2$ - or  $\text{O-CH}_3$  at 3.4–4.0 ppm; line 3:  $\text{C-CH}_2$ - at 2.2–2.4 ppm; line 4:  $\text{-C-CH}_3$  at 1.0–1.3 ppm. Aromatic protons of both structural units gave rise to overlapping signals (line 1) and their intensities were thus integrated. <sup>b</sup> In this table, the numbers of  $^1\text{H}$  atoms are given per TAB building unit. One TAB unit encompasses one TAB plus 1.5 TA-R molecules in perfect structures because each TA-R molecule is connected to two TABs (*cf.* Fig. 1).

observed, which together represented 7% of the total  $^1\text{H}$  intensity (*cf.* Fig. S12 and Table S2, ESI $^\dagger$ ). These signals may, on the one hand, be explained by the aromatic hydroxy groups on 2,5-dihydroxyterephthalaldehyde molecules, since these signals solely occurred in **TAB-TA-OH**, while, on the other hand, the CHO groups of unreacted TA molecules may also contribute to these signals because the  $^1\text{H}$  chemical shift of CHO was predicted to occur at *ca.* 10 ppm. The latter was supported by the observation of a  $^{13}\text{C}$  signal at *ca.* 192 ppm solely for **TAB-TA-OH** (*cf.* Fig. 4). Given the relatively high  $^1\text{H}$  chemical shift beyond 10 ppm, it is tempting to speculate that these protons may be involved in hydrogen bonding with nitrogen atoms, thus forming OH $\cdots$ N moieties. In addition to these  $^1\text{H}$  signals, **TAB-TA-OH** also exhibited relatively intense signals at 1.2 ppm and 3.6 ppm. A plausible explanation for the latter observation may be that the hydroxy groups at least partly reacted with ethanol during solvent exchange, thus forming O-CH $_2$ -CH $_3$  moieties with predicted  $^1\text{H}$  chemical shifts of 3.6 and 1.2 ppm, respectively. In addition, CO-CH $_3$  moieties may also occur as already discussed for **TAB-TA** (see above). The presence of aliphatic edge and/or defect sites was confirmed by the  $^{13}\text{C}$  CP MAS NMR spectra (*cf.* Fig. 4) showing signals in the aliphatic region, which were even more pronounced than for **TAB-TA**. Note that the presence of significant amounts of remaining

solvent molecules adsorbed in the pores was excluded because the samples were rigorously solvent-extracted by the supercritical CO $_2$ -based drying procedure described in the Experimental section.

**TAB-TA-OMe.** For the **TAB-TA-OMe** sample, O-CH $_3$  groups were expected as side groups R (*cf.* Fig. 1). Indeed, the  $^1\text{H}$  MAS NMR spectrum (*cf.* Fig. S13, ESI $^\dagger$ ) showed a signal at the expected chemical shift of 3.6 ppm (line 2) in addition to the broad signal at 6.8 ppm (line 1) due to aromatic  $^1\text{H}$ . Note-worthy, the O-CH $_3$  group  $^1\text{H}$  signal intensity was about 20% higher than expected for the perfect structure (*cf.* Table 1). This could be explained by superimposition with the signal contributions due to edge sites/defects as discussed above. The presence of  $^{13}\text{C}$  signals in the aliphatic region of **TAB-TA-OMe** was also in line with this idea (*cf.* Fig. 4). Note the intense two previously observed signals at 53.7 and 56 ppm due to O-CH $_3$  groups, which could be explained by the presence of the two different stacking modes: AA and AB (*cf.* Fig. 1). Both stacking types were found to be almost equally abundant for the polycrystalline synthesis products, $^{32}$  as confirmed by our spectra (*cf.* Fig. 4).

**TAB-TA-OHex.** In **TAB-TA-OHex** (*cf.* also ESI $^\dagger$  Fig. S14), two intense signals occurred at 3.9 ppm (line 2) and 1.9 ppm (lines 3 + 4) in addition to the dominating signal of the

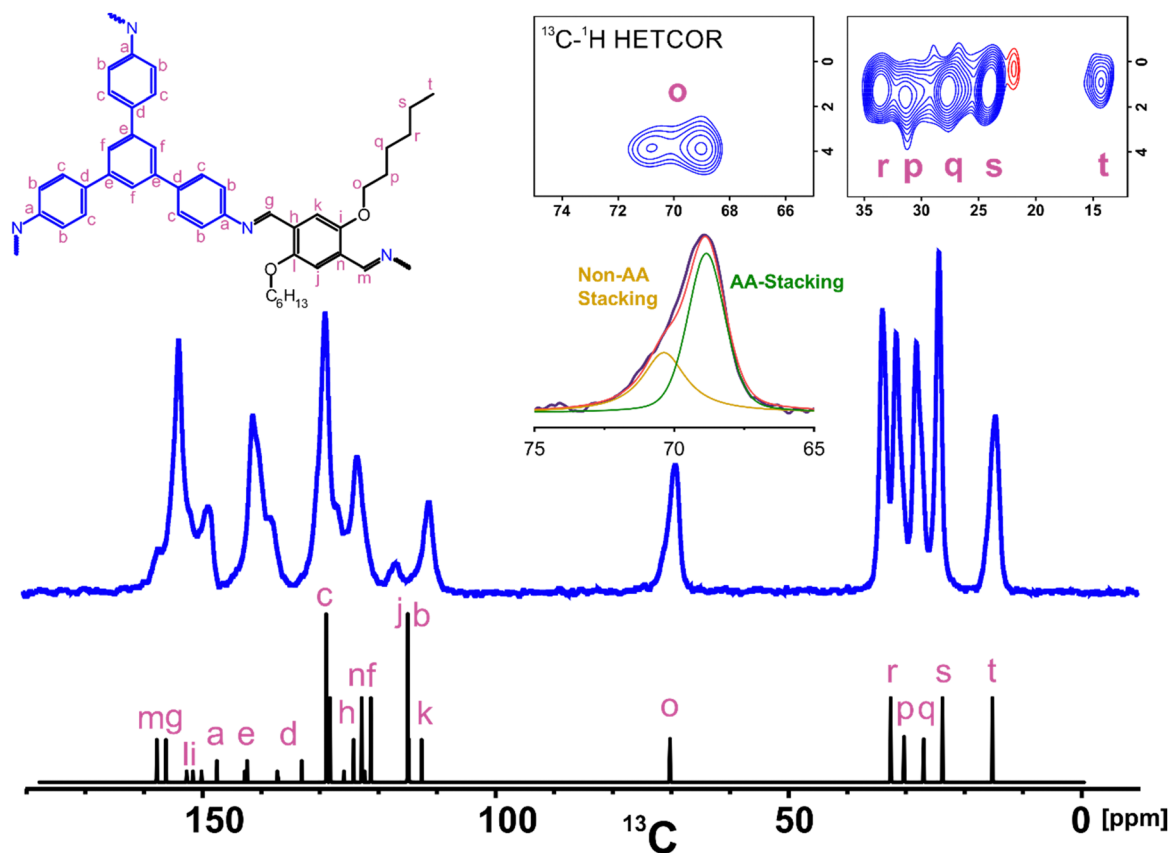


Fig. 5  $^{13}\text{C}$  CP MAS NMR spectrum (blue) with predicted signal positions (black) and sections of the 2D  $^1\text{H}$ - $^{13}\text{C}$  HETCOR spectrum (inserts, top right) for **TAB-TA-OHex** (structure: top middle and left). The full  $^1\text{H}$ - $^{13}\text{C}$  HETCOR spectrum is provided in the ESI $^\dagger$  (Fig. S15). Experimental data were acquired at 800 MHz resonance frequency and a 50 kHz sample spinning rate.

aromatic  $^1\text{H}$  centered at *ca.* 6.4 ppm (line 1). The first two signals were assigned to  $\text{O}-\text{CH}_2-$  groups and  $-\text{C}-(\text{CH}_2)_4-\text{CH}_3$  groups of the hexane side chains, respectively. Note that lines 3 and 4 were not resolved in the  $^1\text{H}$  MAS NMR spectrum of **TAB-TA-OHex** (*cf.* also the insert in Fig. 5 top right) showing the  $^1\text{H}-^{13}\text{C}$  HETCOR spectrum of the OHex side chains. Also, a difference in chemical shift for the overlapping hexane side chain  $\text{C}-\text{CH}_2-$  and  $\text{C}-\text{CH}_3$  groups (lines 3 and 4) was revealed. The measured relative intensities of lines 2 and (3 + 4) slightly exceeded the values expected for a perfect stoichiometric structure (*cf.* Table 1). This could again be explained by superimposition with the signal contributions arising from edge sites/defects (see above). The  $^{13}\text{C}$  CP MAS NMR spectrum of **TAB-TA-OHex** exhibited intense signals of the OHex sidechains in the aliphatic region (see Fig. 4 and 5). The expected six  $^{13}\text{C}$  signals of the OHex side chain could be well resolved and their assignment to the individual carbon positions is given in Fig. 5. The middle insert in Fig. 5 shows the enlarged  $-\text{O}-\text{CH}_2-$  group signal of **TAB-TA-OHex**. As mentioned above, this signal was previously found to be stacking-sensitive for the related compound **TAB-TA-OMe** (*cf.* Fig. 4). For AA stacking, the chemical shifts were about 2.5 ppm lower than for the non-AA stacked structures.<sup>32</sup> For **TAB-TA-OHex**, however, only an asymmetric  $-\text{O}-\text{CH}_2-$  signal was observed instead of two resolved lines. This signal could be decomposed into a more intense narrow signal at 67.6 ppm and a less intense “shoulder” at about 69–70 ppm (see insert in Fig. 5).  $^1\text{H}-^{13}\text{C}$  HETCOR experiments were performed on this sample (Fig. S15, ESI†). The inserted  $^1\text{H}-^{13}\text{C}$  HETCOR section (Fig. 5, top middle) clearly demonstrated the presence of two signals at the expected positions, which justified the decomposition of the 1D  $^{13}\text{C}$  CP MAS NMR spectrum. The higher intensity of the narrow signal at 67.6 ppm indicated that AA stacking was preferred in **TAB-TA-OHex**. Note, however, that the intensities of CP spectra are usually not quantitative because the  $^1\text{H}-^{13}\text{C}$  polarization transfer efficiencies may differ for different signals.<sup>46</sup> We were thus hesitant to provide percentages for the two stacking modes. Given the fact that the two signals were due to carbons in similar environments, we could, however, assume comparable cross-polarization efficiencies. This justifies at least the semi-quantitative statement of a significantly higher intensity for the signal at 67.6 ppm. The AA stacking type was here preferred, probably because the long hexoxy side chains were spatially more demanding than the methyl groups of **TAB-TA-OMe**. For comparison, the  $^1\text{H}-^{13}\text{C}$  HETCOR spectrum of **TAB-TA-OMe** is also provided in ESI† (Fig. S16). The cross-peak due to  $\text{O}-\text{Me}$  was clearly split into the two expected signals due to AA and AB stacking.

As mentioned above, the relative intensity of lines 2 and (3 + 4) centered around 3.9 and 1.9 ppm was slightly higher than expected for a perfect structure. This implied a contribution of edge sites/defects to these two signals as already described for the other compounds. Their presence could, however, not be confirmed by  $^{13}\text{C}$  CP MAS NMR spectroscopy for **TAB-TA-OHex** because the  $^{13}\text{C}$  signals of the OHex sidechains dominate the aliphatic region and may cover the minor signals due to edge sites/defects in contrast to the other compounds studied here.

However,  $^{13}\text{C}-^1\text{H}$  HETCOR spectroscopy (see the right insert in Fig. 5) revealed the presence of at least one additional cross-peak at 0.5 ppm  $^1\text{H}$  and 21.9 ppm  $^{13}\text{C}$  chemical shift as indicated. Two explanations are possible: (i) this cross-peak may be due to the smaller sample fraction with AB stacking; (ii) it could also indicate edge sites/defects. The  $^1\text{H}$  chemical shift of less than 1 ppm, however, rather pointed toward edge sites or defects.

## 4. Conclusions

In summary, high-field and fast-spinning  $^1\text{H}$  MAS NMR spectroscopy allowed the detection and quantification of various  $^1\text{H}$  sites present in 2D COF materials. In addition to the expected signals of aromatic groups and side chain  $^1\text{H}$ , several  $^1\text{H}$  signals at chemical shifts between *ca.* 1 and 4 ppm could be resolved and assigned to edge sites and/or defects (*cf.* Fig. 3 and Table 1). Signals in this range were indicative of  $\text{OCH}_x$ ,  $\text{CH}_2$ , and  $\text{CH}_3$  groups, which may have been formed at the edges of 2D layers or on defects within the layers, *e.g.*, by side-reactions with solvent constituents. To date, solid-state NMR spectrometers operating at field strengths corresponding to 1.2 GHz  $^1\text{H}$  resonance frequency<sup>47</sup> as well as MAS probes with maximum sample spinning rates well beyond 100 kHz<sup>48,49</sup> are available. This may in the future even allow resolving overlapping signals of the different aromatic  $^1\text{H}$  groups contributing to line 1 at about 7 ppm. It is thus likely that the  $^1\text{H}$  MAS NMR spectroscopy of 2D COFs will become an important tool for their structure characterization. Moreover, these developments will increasingly enable the application of various  $^1\text{H}$ -detected 2D correlation experiments, like  $^1\text{H}-^1\text{H}$ ,  $^1\text{H}-^{13}\text{C}$ , and others as described<sup>50–53</sup> and reviewed<sup>54</sup> in the recent literature, thus paving the way to the future in-depth structural characterization of 2D COFs.

## Author contributions

Ankita De and Andreas Schneemann synthesized the 2D COFs, characterized them with PXRD and FTIR measurements and described their morphology with SEM. Nikolaj Lopatik and Silvia Paasch have characterized structures of 2D COFs with solid-state NMR spectroscopy. Eike Brunner has supervised the NMR spectroscopic studies. All authors contributed to data interpretation and checked the experimental data. All authors contributed to paper writing, edited, and approved the final version of the manuscript.

## Conflicts of interest

There are no conflicts to declare.

## Acknowledgements

The authors gratefully acknowledge financial support from the collaborative research center (CRC) 1415 “Chemistry of

Synthetic 2D Materials” funded by the Deutsche Forschungsgemeinschaft (DFG, German Research Foundation)—SFB-1415-417590517 (subprojects A02 and B01). AS gratefully acknowledges the Fonds der chemischen Industrie for a Liebig Fellowship.

## References

- 1 A. K. Geim and K. Novoselov, *Nat. Mater.*, 2007, **6**, 183–191.
- 2 A. Dideikin and A. Vul', *Front. Phys.*, 2019, **6**, 149.
- 3 P. Feicht, R. Siegel, H. Thurn, J. W. Neubauer, M. Seuss, T. Szabó, A. V. Talyzin, C. E. Halbig, S. Eigler, D. A. Kunz, A. F. G. Papastavrou, J. Senker and J. Breu, *Carbon*, 2017, **114**, 700–705.
- 4 K. Zhang, Y. Feng, F. Wang, Z. Yang and J. Wang, *J. Mater. Chem. C*, 2017, **5**, 11992–12022.
- 5 B. Aufray, A. Kara, S. Vizzini, H. Oughaddou, C. Léandri, B. Ealet and G. Le Lay, *Appl. Phys. Lett.*, 2010, **96**, 183102.
- 6 M. E. Dávila, L. Xian, S. Cahangirov, A. Rubio and G. Le Lay, *New J. Phys.*, 2014, **16**, 095002.
- 7 Y. Xu, B. Yan, H.-J. Zhang, J. Wang, G. Xu, P. Tang, W. Duan and S. C. Zhang, *Phys. Rev. Lett.*, 2013, **111**, 136804.
- 8 H. Liu, A. T. Neal, Z. Zhu, Z. Luo, X. Xu, D. Tománek and P. D. Ye, *ACS Nano*, 2014, **8**, 4033–4041.
- 9 M. Naguib, M. Kurtoglu, V. Presser, J. Lu, J. Niu, M. Heon, L. Hultman, Y. Gogotsi and M. W. Barsoum, *Adv. Mater.*, 2011, **23**, 4248–4253.
- 10 B. Anasori, M. Lukatskaya and Y. Gogotsi, *Nat. Rev. Mater.*, 2017, **2**, 16098.
- 11 M. A. Hope, A. C. Forse, K. J. Griffith, M. R. Lukatskaya, M. Ghidui, Y. Gogotsi and C. P. Grey, *Phys. Chem. Chem. Phys.*, 2016, **18**, 5099–5102.
- 12 M. J. Cliffe, E. Castillo-Martínez, Y. Wu, J. Lee, A. C. Forse, F. C. N. Firth, P. Z. Moghadam, D. Fairen-Jimenez, M. W. Gaultois, J. A. Hill, O. V. Magdysyuk, B. Slater, A. L. Goodwin and C. P. Grey, *J. Am. Chem. Soc.*, 2017, **139**, 5397–5404.
- 13 A. Schneemann, R. Dong, F. Schwotzer, H. Zhong, I. Senkovska, X. Feng and S. Kaskel, *Chem. Sci.*, 2021, **12**, 1600–1619.
- 14 X. Liu, C. Guan, S. Ding, W. Wang, H. Yan, D. Wang and L. Wan, *J. Am. Chem. Soc.*, 2013, **135**, 10470–10474.
- 15 H. Xu, J. Gao and D. Jiang, *Nat. Chem.*, 2015, **7**, 905–912.
- 16 B. Lukose, A. Kuc and T. Heine, *Chem. – Eur. J.*, 2011, **17**, 2388–2392.
- 17 J. Yang, A. Acharjya, M. Ye, J. Rabeah, S. Li, Z. Kochovski, S. Youk, J. Roeser, J. Grüneberg, C. Penschke, M. Schwarze, T. Wang, Y. Lu, R. van de Krol, M. Oschatz, R. Schomäcker, P. Saalfrank and A. Thomas, *Angew. Chem., Int. Ed.*, 2021, **60**, 1997–19803.
- 18 D. Shinde, G. Sheng, X. Li, M. Ostwal, A. Emwas, K. Huang and Z. Lai, *J. Am. Chem. Soc.*, 2018, **140**(43), 14342–14349.
- 19 S. Haldar, K. Roy, R. Kushwaha, S. Ogale and R. Vaidhyanathan, *Adv. Energy Mater.*, 2019, **9**, 1902428.
- 20 D. Pastoetter, S. Xu, M. Borrelli, M. Addicoat, B. Biswal, S. Paasch, A. Dianat, H. Thomas, R. Berger, S. Reineke, E. Brunner, G. Cuniberti, M. Richter and X. Feng, *Angew. Chem., Int. Ed.*, 2020, **59**, 23620–23625.
- 21 H. Nguyen, *Chem. Sci.*, 2021, **12**, 8632–8647.
- 22 F. Haase and B. Lotsch, *Chem. Soc. Rev.*, 2020, **49**, 8469–8500.
- 23 M. Duer, *Solid state NMR spectroscopy: principles and applications*, John Wiley & Sons, 2008.
- 24 A. Côté, A. Benin, N. Ockwig, M. O'Keeffe, A. Matzger and O. Yaghi, *Science*, 2005, **310**, 1166–1170.
- 25 W. Cai, R. Piner, F. Stadermann, S. Park, M. Shaibat, Y. Ishii, D. Yang, A. Velamakanni, S. An, M. Stoller, J. An, D. Chen and R. Ruoff, *Science*, 2008, **321**, 1815–1817.
- 26 A. MacIntosh, K. Harris and G. Goward, *Chem. Mater.*, 2016, **28**, 360–367.
- 27 I. Vacchi, C. Spinato, J. Raya, A. Bianco and C. Ménard-Moyon, *Nanoscale*, 2016, **8**, 13714–13721.
- 28 X. Wu, B. Wang, Z. Yang and L. Chen, *J. Mater. Chem. A*, 2019, **7**, 5650–5655.
- 29 S. Bügel, M. Hähnel, T. Kunde, N. de Sousa Amadeu, Y. Sun, A. Spieß, T. H. Y. Beglau, B. M. Schmidt and C. Janiak, *Materials*, 2022, **15**, 2807.
- 30 D. L. Pastoetter, Y. Liu, M. A. Addicoat, S. Paasch, A. Dianat, D. Bodesheim, A. L. Waentig, S. Xu, M. Borrelli, A. Croy, M. Richter, E. Brunner, G. Cuniberti and X. Feng, *Chem. – Eur. J.*, 2022, e202104502.
- 31 B. Sun, Q. Lu, K. Chen, W. Zheng, Z. Liao, N. Lopatik, D. Li, M. Hantusch, S. Zhou, H. I. Wang, Z. Sofer, E. Brunner, E. Zschech, M. Bonn, R. Dronskowski, D. Mikhailova, Q. Liu, D. Zhang, M. Yu and X. Feng, *Adv. Mater.*, 2022, 2108682.
- 32 C. Kang, Z. Zhang, A. K. Usadi, D. C. Kalabro, L. Saunders Baugh, K. Yu, Y. Wang and D. Zhao, *J. Am. Chem. Soc.*, 2022, **144**, 3192–3199.
- 33 A. De, S. Haldar, S. Michel, L. Shupletsov, V. Bon, N. Lopatik, L. Ding, L. M. Eng, G. K. Auernhammer, E. Brunner and A. Schneemann, *Chem. Mater.*, 2023, **35**, 3911–3922.
- 34 B. Zhang, H. Mao, R. Matheu, J. Reimer, S. A. Alshimri, S. Alshihri and O. Yaghi, *J. Am. Chem. Soc.*, 2019, **141**, 11420–11424.
- 35 Q. Sun, B. Aguila, J. Perman, L. D. Earl, C. W. Abney, Y. Cheng, H. Wei, N. Nguyen, L. Wojtas and S. Ma, *J. Am. Chem. Soc.*, 2017, **139**, 2786–2793.
- 36 Q. Sun, Y. Tang, B. Aguila, S. Wang, F.-S. Xiao, P. K. Thallapally, A. M. Al-Enizi, A. Nafady and S. Ma, *Angew. Chem., Int. Ed.*, 2019, **58**, 8670.
- 37 P. Shao, J. Li, F. Chen, L. Ma, Q. Li, M. Zhang, J. Zhou, A. Yin, X. Feng and B. Wang, *Angew. Chem., Int. Ed.*, 2018, **57**, 16501.
- 38 C. Feriante, A. Evans, S. Jhulki, I. Castano, M. Strauss, S. Barlow, W. Dichtel and S. Marder, *J. Am. Chem. Soc.*, 2020, **142**(43), 18637–18644.
- 39 S. Jhulki, A. Evans, X. Hao, M. Cooper, C. Feriante, J. Leisen, H. Li, D. Lam, M. Hersam, S. Barlow, J. Brédas, W. Dichtel and S. Marder, *J. Am. Chem. Soc.*, 2020, **142**(2), 783–791.
- 40 NMR predictors. ACD/Labs. (2022, July 5). Retrieved October 7, 2022, from <https://www.acdlabs.com/products/spectrus-platform/nmr-predictors>.



- 41 E. Brunner, D. Freude, B. Gerstein and H. Pfeifer, *J. Magn. Reson.*, 1990, **90**, 90–99.
- 42 E. Brunner, D. Fenzke, D. Freude and H. Pfeifer, *Chem. Phys. Lett.*, 1990, **169**, 591–594.
- 43 M. Alla and E. Lippmaa, *Chem. Phys. Lett.*, 1982, **87**, 30–33.
- 44 U. Schwark, D. Michel and M. Pruski, *J. Magn. Reson., Ser. A*, 1996, **119**, 157–164.
- 45 A. Hofstetter, M. Balodis, F. M. Paruzzo, C. M. Widdifield, G. Stevanato, A. C. Pinon, P. J. Bygrave, G. M. Day and L. Emsley, *J. Am. Chem. Soc.*, 2019, **141**, 16624–16634.
- 46 D. Schulze, H. Ernst, D. Fenzke, W. Meiler and H. Pfeifer, *J. Phys. Chem.*, 1990, **94**, 3499–3502.
- 47 M. Callon, A. Malär, S. Pfister, V. Římal, M. Weber, T. Wiegand, J. Zehnder, M. Chávez, R. Cadalbert, R. Deb, A. Däpp, M. Fogeron, A. Hunkeler, L. Lecoq, A. Torosyan, D. Zyla, R. Glockshuber, S. Jonas, M. Nassal, M. Ernst, A. Böckmann and B. Meier, *J. Biomol. NMR*, 2021, **75**, 255–272.
- 48 S. Penzel, A. Oss, M. Org, A. Samoson, A. Böckmann, M. Ernst and B. Meier, *J. Biomol. NMR*, 2019, **73**, 19–29.
- 49 J. Struppe, C. Quinn, S. Sarkar, A. Gronenborn and T. Polenova, *Mol. Pharmaceutics*, 2020, **17**, 674–682.
- 50 X. Lu, Y. Tsutsumi, C. Huang, W. Xu, S. R. Burn, A. C. Templeton, A. V. Buevich, J.-P. Amoureux and Y. Su, *Phys. Chem. Chem. Phys.*, 2020, **22**, 13160–13170.
- 51 M. Li, F. Meng, Y. Tsutsumi, J.-P. Amoureux, W. Xu, X. Lu, F. Zhang and Y. Su, *Mol. Pharmaceutics*, 2020, **17**, 2196–2207.
- 52 C. Rehman, W. T. Franks, B. Nguyen, H. F. Schmidt, G. Scrivens and S. P. Brown, *J. Pharm. Sci.*, 2023, **112**, 1915–1928.
- 53 E. Bartalucci, A. A. Malär, A. Mehnert, J. B. Kleine-Büning, L. Günzel, M. Icker, M. Börner, C. Wiebeler, B. H. Meier, S. Grimme, B. Kersting and T. Wiegand, *Angew. Chem., Int. Ed.*, 2023, **62**, e202217725.
- 54 Y. Nishiyama, G. Hou, V. Agarwal, Y. Su and A. Ramamoorthy, *Chem. Rev.*, 2023, **123**, 918–988.